Cobalt@Nitrogen-Doped Porous Carbon Fiber Derived from the Electrospun Fiber of Bimetal–Organic Framework for Highly Active Oxygen Reduction

Qing Bai, Feng-Cui Shen, Shun-Li Li, Jiang Liu, Long-Zhang Dong, Zeng-Mei Wang,* and Ya-Qian Lan*

The exploitation of high-efficiency, cost-effective, and stable oxygen reduction reaction (ORR) electrocatalysts is extremely critical for energy storage and conversion technology. The transition metal carbonitrides have been investigated as an alternative to precious metal-based catalysts. Here, a series of uniform Co nanoparticles encapsulated in nitrogen-doped porous carbon fibers (Co@N-PCFs for brevity) are designed and synthesized by directly carbonizing the Zn_xCo_{1-x}-zeolitic imidazolate frameworks@polyacrylonitrile (Zn_xCo_{1-x}-ZIFs@PAN) electrospun nanofibers. By precisely controlling the Zn/Co molar ratio in the Zn_xCo_{1-x}-ZIFs precursor and carbonization temperature, a higher activity and stability ORR catalyst of Co@N-PCF-3 is prepared. The results reveal that Co@N-PCF-3 exhibits outstanding ORR activity outperformed commercial Pt/C with more positive half-wave potential of −134 mV versus Ag/AgCl, high selectivity to four-electron pathway ($n \approx 3.9$), as well as remarkable stability and methanol tolerance. Remarkably, it is one of the highest ORR catalysts among the cobalt carbonitrides reported in the literature.

1. Introduction

Oxygen reduction reaction (ORR) is known as the most important cathodic reaction process for energy storage and transformation in such devices as metal–air batteries[1,2] and fuel cells.[3] Up to now, Pt-based electrocatalysts have been extensively considered to be the most active ORR electrocatalysts in electrochemical cell reactions.[4–6] Nevertheless, crustal rarity, high cost, poor stability, and methanol crossover of Pt-based materials and the sluggish kinetics of cathodic reaction greatly restrict their large-scale practical application. In this connection, a great deal of investigation has been performed based on the study of efficient non-noble metal catalysts, which mainly consists of non-noble metal compounds (e.g., oxides, nitrides, phosphide, and chalcogenides), metal-free catalysts as well as carbonitrides.[7–11] Then, the transition metal carbonitrides (TM-N-C, where TM represents mainly Co, Fe), obtained by carbonization various nitrogen-rich precursor (such as dicyandiamide, melamine, polyaniline, and metal–organic frameworks (MOFs)), have been widely explored to substitute precious metal catalysts because of their high catalytic activity and durability in acid or alkaline electrolyte.[12–15]

In recent years, MOFs have been served as precursors to fabricate the functional nanostructured porous carbon-based electrocatalysts, which gives the credit to their excellent intrinsic characteristics, such as large specific surface area derived from the porosity and the diversity of structure and function stemmed from different metal ions and organic ligands.[16–22] In particular, Zn-Co bimetallic ZIFs (BMZIFs (ZIF-67 and ZIF-8)) have been extensively employed as precursors to develop efficient Co-based porous nitrogen-doped carbon catalysts,[22–24] which attributes to their unique merits. I) Co-N_x sites can be easily produced by pyrolysis due to Co metal directly connected to N species.[25,26] II) The larger surface area derived from the pore structure, due to the evaporation of Zn at high temperature.[27,28] III) Uniform N atoms doped into the obtained carbon skeleton after calcination of Zn-ZIF.[29] However, the skeleton of MOFs was generally prone to collapse and aggregate in the pyrolysis process (>700 °C),[17,30] resulting in fewer pore structures, which greatly reduces the electrochemical performance. Therefore, it is urgent and significant to assist the MOFs with quite a few novel substrates (e.g., layered double hydroxides (LDHs),[30,31] graphene,[21] carbon cloth,[32] polyacrylonitrile (PAN) nanofibers,[33] and Te nanowires[29]) to achieve the

Q. Bai, Prof. Z.-M. Wang
Jiangsu Key Laboratory of Construction Materials
College of Materials Science and Engineering
Southeast University
Nanjing 211189, P. R. China
E-mail: 101011338@seu.edu.cn
Dr. F.-C. Shen, Dr. S.-L. Li, Dr. J. Liu, L.-Z. Dong, Prof. Y.-Q. Lan
Jiangsu Key Laboratory of Biofunctional Materials
College of Chemistry and Materials Science
Nanjing Normal University
Nanjing 210023, P. R. China
E-mail: yqlan@njnu.edu.cn
Dr. F.-C. Shen
College of Biological and Chemical Engineering
Anhui Polytechnic University
Wuhu 241000, P. R. China

**ADVANCED
SCIENCE NEWS**
www.advancedsciencenews.com
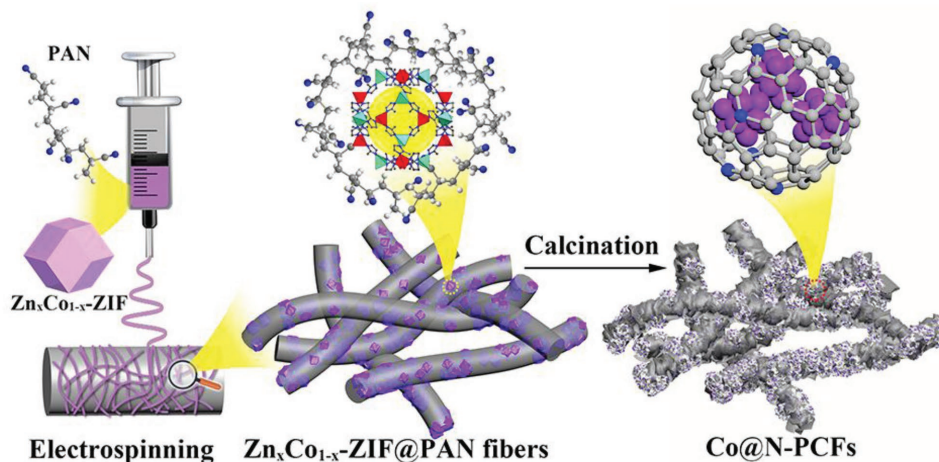
**small
methods**
www.small-methods.com

Figure 1. Schematic preparation process of Co@N-PCFs nanocomposite.

orderly stacking of carbon-based materials and the generation of porous structures in the pyrolysis process. Unfortunately, the preparation method of graphene is complex and the yield is low, and the LDHs possess chemical activity but cannot improve the conductivity of the material.[34] By contrast, the PAN fibers prepared by electrospinning have great advantages, its preparation method is simple, electrospinning fibers have high porosity and good uniformity, and the carbonized fibers have a larger specific area, conductivity, and a high yield.

In view of the foregoing, we rationally designed and synthesized 1D Zn_xCo_{1-x}-ZIFs@PAN fibers by electrospinning, in which PAN fibers acted as an excellent template for the uniform distribution of Zn_xCo_{1-x}-ZIFs. Through the pyrolysis process, the PAN fibers converted into carbon fibers with excellent electrical conductivity, which is highly desirable for the ORR catalysts. Meanwhile, the degree of graphitization, the content of Co-N_x active sites, and N-doped carbon in the resultant pyrolysis products as well as the porosity of catalysts can be precisely controlled by effectively adjusting Zn/Co molar ratio (x value) in Zn_xCo_{1-x}-ZIFs. By adjusting the Zn/Co molar ratio and the pyrolysis temperature, the optimal Co@N-PCF-3 exhibits excellent ORR catalytic activity (with a more positive half-wave potential of −134 mV vs Ag/AgCl and the electron transfer number ≈3.9) superior to the commercial Pt/C (corresponding to −169 mV vs Ag/AgCl and ≈3.85, respectively).

2. Results and Discussion

The synthesis process of the Co@N-PCFs catalysts is schematically depicted in **Figure 1** involving the synthesis of Zn_xCo_{1-x}-ZIFs (x is the molar ratio of Zn^{2+} in Zn^{2+} Co^{2+}; x = 1, 0.67, 0.5, 0.33, and 0, respectively), electrospinning, and pyrolysis. First of all, Zn_xCo_{1-x}-ZIFs were synthesized in accordance with the previously reported method.[35] Then, 1D Zn_xCo_{1-x}-ZIFs@PAN was synthesized by a straightforward electrospinning method with Zn_xCo_{1-x}-ZIFs and PAN as raw materials, in which the PAN not only played a role in regulating viscosity, but also was the carbon source of the carbon fibers. Upon carbonizing at 900 °C for 3 h under N_2 atmosphere with 3 °C min^{-1}, the

final samples denoted as Co@N-PCF-1-5, respectively, corresponding to the pyrolysis products of Zn_xCo_{1-x}-ZIFs@PAN, x = 1, 0.67, 0.5, 0.33, and 0 were obtained. In controlled experiments, various carbonized products of $Zn_{0.5}Co_{0.5}$-ZIF@PAN at different pyrolysis temperature (800 °C, 1000 °C corresponding to Co@N-PCF-6, 7, respectively) and $Zn_{0.5}Co_{0.5}$-ZIF at 900 °C (short for Co-C-N) were further investigated in alkaline electrolyte (0.1 M KOH) (see Experimental Section in the Supporting Information).

The phase composition and crystallinity of Co@N-PCFs prepared with various Zn/Co molar ratios in Zn_xCo_{1-x}-ZIFs precursors were revealed by powder X-ray diffraction (PXRD). In **Figure 2**a and Figure S1a (Supporting Information), the broad diffraction peak located at ≈25° was matched with the (002) crystal plane of graphite carbon, deriving from the porous carbon fibers obtained from the pyrolysis of the Zn_xCo_{1-x}-ZIFs@PAN fibers. The other diffraction peaks at 44.37°, 51.59°, and 76.08° are consistent with the (111), (200), and (220) crystal planes of face-centered cubic metallic Co (JCPDS No. 15–806), and the diffraction peaks of Co were gradually appeared and enhanced with the increase of Co content, corresponding to energy-dispersive spectrometer (EDX, Figure S2 and Table S1, Supporting Information). In addition, the relevant comparison also revealed the distinct peaks of Co phase (Figures S1b and S15a, Supporting Information). For the purpose of obtaining the morphology and composition of the precursors, scanning electron microscopy (SEM), transmission electron microscopy (TEM), PXRD, and EDX characterizations were performed. Both the TEM (Figure 2b) and SEM (Figure S3b, Supporting Information) of $Zn_{0.5}Co_{0.5}$-ZIF indicated that the obtained precursors possessed a uniform dodecahedral morphology with average size of ≈150 nm. The X-ray diffraction (XRD) patterns shown in Figure S3a (Supporting Information) demonstrated that Zn_xCo_{1-x}-ZIFs have a similar zeolite structure and a higher crystallinity, and the EDX spectrums (Figure S4, Supporting Information) witness the presence of Zn, Co element. Figure 2c shows the SEM images of $Zn_{0.5}Co_{0.5}$-ZIF@PAN fibers with a diameter of ≈1 μm obtained by electrospinning the sol with PAN and $Zn_{0.5}Co_{0.5}$-ZIF as raw materials. As observed from the inset of Figure 2c, the dodecahedral $Zn_{0.5}Co_{0.5}$-ZIF particles

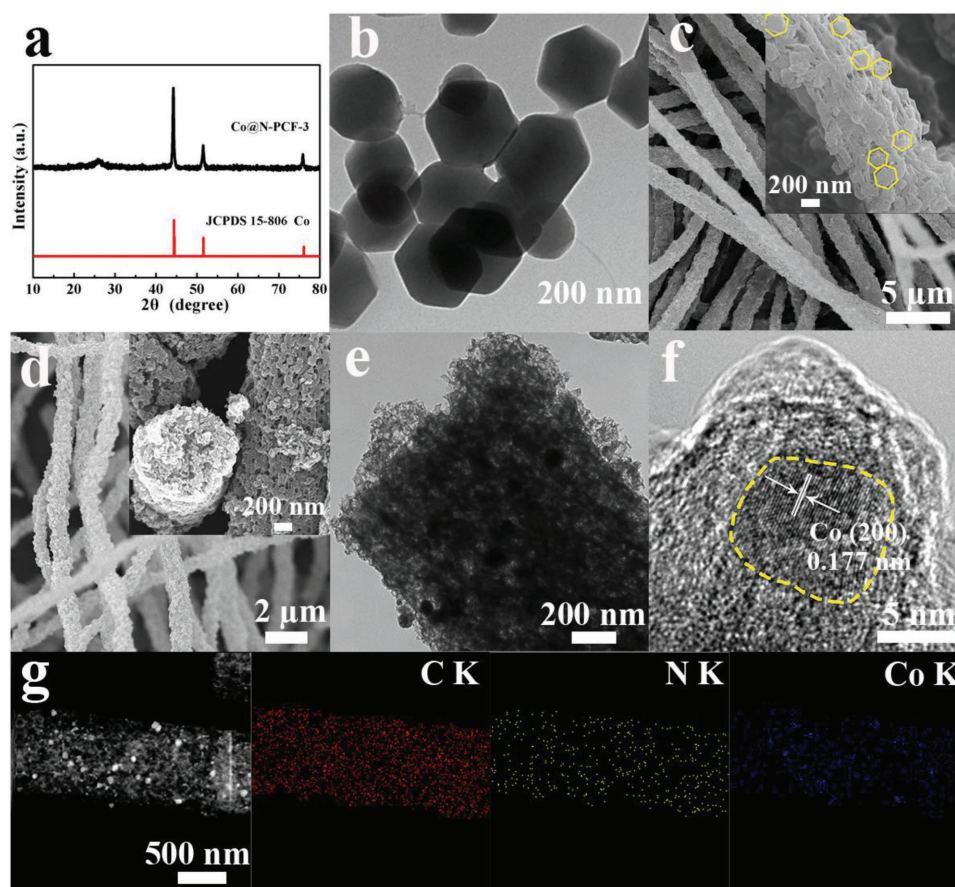**Figure 2.** a) XRD pattern of Co@N-PCF-3. b) TEM image of the $Zn_{0.5}Co_{0.5}$-ZIF. c) SEM images of the $Zn_{0.5}Co_{0.5}$-ZIF@PAN fiber. d) SEM images, e) TEM image, f) HRTEM image, and g) corresponding element mapping of Co@N-PCF-3.

were evenly distributed on the surface and the interior of the fibers, demonstrating that the $Zn_{0.5}Co_{0.5}$-ZIF particles were successfully introduced into the PAN fibers. After carbonization at 900 °C, the $Zn_{0.5}Co_{0.5}$-ZIF@PAN fibers were converted into Co@N-PCF-3 with a slight shrink in the diameter (Figure 2d), owing to the volatilization of noncarbon components in PAN during pyrolysis process. Lots of pore structure uniformly distributed on the fibers surface and cross-section, which gives the credit to the fact that the Zn^{2+} was reduced to Zn by carbon and evaporate at high temperature during the calcining process.[28] The result was further confirmed by TEM images in Figure 2e and Table S2 (Supporting Information). As shown in the TEM images, metallic nanoparticles (NPs are mainly Co) and pore structure uniformly distributed in Co@N-PCF-3 fibers can effectively promote the ORR activity owing to the improved electron and mass conductivity.[23] Compared with other Co@N-PCFs samples (Table S2, Supporting Information), the pore structure gradually decreased and the number of Co NPs increased with the decrease of Zn^{2+} molar ratio. The nanostructure of Co@N-PCF-3 was also investigated by high-resolution TEM (HRTEM), where the clear lattice fringe spacing of 0.177 nm corresponding to the (200) planes of Co (Figure 2f) can be seen. Moreover, element mapping for Co@N-PCF-3 (Figure 2g) was indicative of the uniform distribution of C, N, and Co elements.

To investigate the surface valence state and element bonding composition of the as-prepared sample Co@N-PCF-3, the X-ray photoelectron spectroscopy (XPS) measurement was performed. As revealed in **Figure 3**a, the full XPS spectrum showed peaks of C 1s, N 1s, O 1s, and Co 2p. The Co 2p spectrum (see Figure 3b) was further analyzed by deconvolution, the high-resolution spectra of Co $2p_{3/2}$ and $2p_{1/2}$ matched with Co°, Co(II), and the satellite peaks, respectively. The peak at 780.04 eV (Co $2p_{3/2}$) corresponds to the zero-valent Co (Co°). The peaks at 781.12 and 796.36 eV ascribed to the Co $2p_{3/2}$ and Co $2p_{1/2}$ of Co^{2+}, attributing to the surface oxidation of the catalysts. The satellite peaks were detected at 785.78 and 802.11 eV.[36] The high-resolution C 1s XPS spectrum (Figure 3c) included three subpeaks: C-C sp^2 (284.6 eV), C-C sp^3 (285.7 eV), and C = N/C = O (287.6 eV).[37,38] Furthermore, the N 1s XPS spectrum shown in Figure 3d can be fitted by five types of nitrogen species: pyridinic N (398.5 eV, 29.64 %), Co-N_x (399.5 eV, 19.67%), pyrrolic N (399.7 eV, 11.10%), graphitic N (400.8 eV, 20.51%), and oxidized N (402.0 eV, 19.08%).[39] The previous reports proposed that the N-doped carbon catalysts with high content of pyridinic N and graphitic N exhibit excellent oxygen reduction catalytic performance, owing to the fact that the pyridinic N improves the onset potential and the graphitic N enhances the limiting current density.[40,41] Moreover, the catalysts containing Co-N_x moieties can effectively

**ADVANCED
SCIENCE NEWS**
www.advancedsciencenews.com
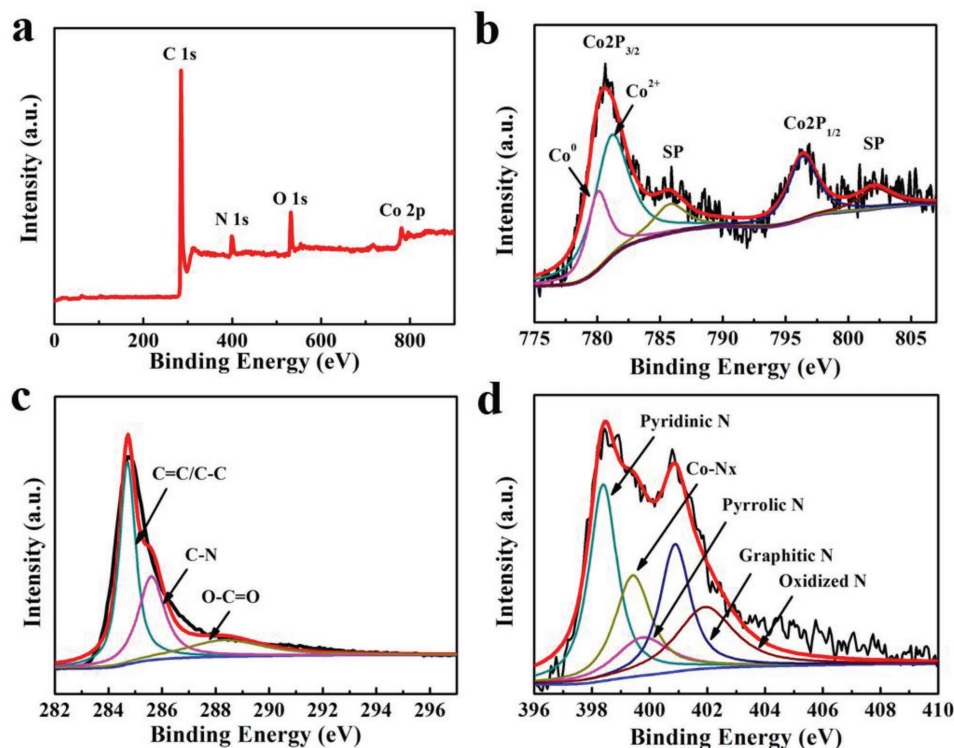
**small
methods**
www.small-methods.com

Figure 3. XPS spectrum of a) Co@N-PCF-3. High-resolution scans of b) Co 2p, c) C 1s, and d) N 1s electrons of Co@N-PCF-3.

improve the ORR activity, especially the uniformly distributed Co-N$_x$ moieties.[42] Raman spectrum was investigated to further verify the formation of graphitic carbon for Co@N-PCFs (Figure S5, Supporting Information). The intensity ratio of D band to G band (I_D/I_G) for Co@N-PCF-1-5 decreases from 1.02 to 0.98 with the increase of Co^{2+} molar ratio from 0 to 1, implied that the higher graphitic degree and fewer defects were present at the higher Co^{2+} molar ratio.[30] The I_D/I_G values of Co@N-PCF-6, 3, and 7 obtained at 800, 900, and 1000 °C are 1.08, 1.00, and 0.79, respectively, signifying the graphitic structure can generate more at high temperature. The surface area of Co@N-PCF-1-5 and corresponding pore structures were characterized by N$_2$-adsorption/desorption measurements (see Figures S6 and S7, Supporting Information). Representative IV-type isotherms and H4-type hysteresis loops are observed for all the catalysts. Brunauer–Emmett–Teller (BET) method was carried out to analyze the specific surface area of Co@N-PCF-1-7. It turned out that BET surface area decreases significantly from 582 m^2 g^{-1} (Co@N-PCF-1) to 260 m^2 g^{-1} (Co@N-PCF-5) with the reduction of Zn^{2+} molar ratio, as well as the surface area increase first and then decrease as the temperature rising from 800 to 1000 °C, which is consistent with previous consequence that Zn evaporated during the calcining process and the pores left. The pore size distribution for a series of Co@N-PCFs (Figure S6b, Supporting Information) was obtained by the Barrett–Joyner–Halenda model, indicating the mesoporous structures (3–7 nm). The numerous mesoporous derived from the evaporation of Zn[27,29] contributes significantly to the exposure of Co-N$_x$ active sites and mass transport of O$_2$, H$_2$O, and OH$^-$.[25,43] The results indicate that Zn element in Zn$_x$Co$_{1-x}$-ZIF@PAN precursors facilitates the formation of

porous carbon and the doping of N, while the introduction of Co element improves the degree of graphitization and electrical conductivity of Co@N-PCFs, which together benefits to improving the ORR catalytic activity.

Subsequently, the ORR performance for the samples carbonized at 900 °C with different Zn^{2+}, Co^{2+} molar ratio in precursors was primarily investigated on the rotating disk electrode (RDE). Cyclic voltammetry (CV) curves of Co@N-PCF-3 were first performed in N$_2$-and O$_2$-saturated 0.1 M KOH solution. The results shown in Figure S8 (Supporting Information) indicated that a significant cathodic peak with a positive peak potential for Co@N-PCF-3 was measured appearing in O$_2$-saturated electrolyte, whereas there was no reduction peak in the N$_2$-saturated KOH solution, which shows the performance of Co@N-PCF-3 for ORR. The CV curves for series of Co@N-PCF were also examined in O$_2$-saturated 0.1 M KOH and shown in **Figure 4**a. It is noteworthy that the reduction peak potential at –0.177 V (vs Ag/AgCl) for Co@N-PCF-3 is more positive than that of Co@N-PCF-1 (–0.248 V), Co@N-PCF-2 (–0.183 V), Co@N-PCF-4 (–0.19 V), Co@N-PCF-5 (–0.201 V), and Pt/C (–0.191 V), demonstrating that the ORR activity of Co@N-PCF-3 is superior to other Co@N-PCF samples and Pt/C. The ORR performance of Co@N-PCF-1-5 and Pt/C catalysts was further investigated by linear sweep voltammetry (LSV). As shown in Figure 4b and Table S3 (Supporting Information), the best ORR catalytic performance was achieved by Co@N-PCF-3 owing a larger positively onset potential (E_{onset}, –46 mV vs Ag/AgCl) and half-wave potential ($E_{1/2}$, –134 mV vs Ag/AgCl) as well as higher diffusion-limiting current density (J_L, 5.09 mA cm^{-2}). Remarkably, the ORR catalytic activity of Co@N-PCF-3 was not only better than that of other Co@N-PCFs samples, but
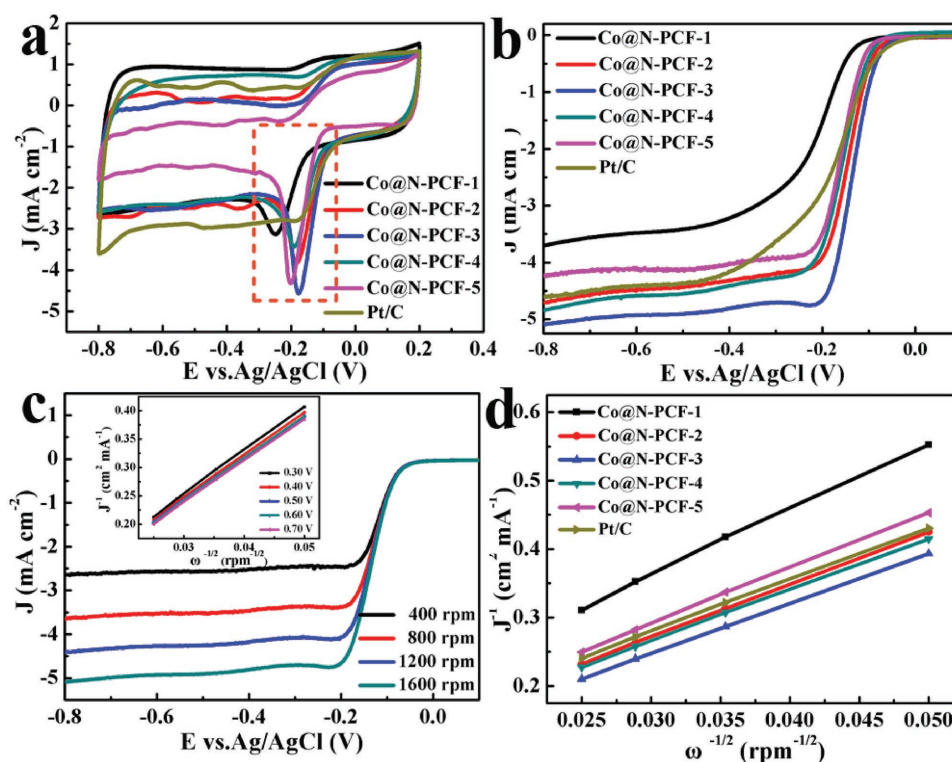
ADVANCED
SCIENCE NEWS
www.advancedsciencenews.com

small
methods
www.small-methods.com

Figure 4. Electrochemical properties of a) CV curves of Co@N-PCF-1-5 (with different Co^{2+} molar ratio) obtained at 900 °C in O_2-saturated 0.1 M KOH electrolyte with a scan rate of 100 mV s^{-1}. b) LSV curves of Co@N-PCF-1-5 and 20% Pt/C catalyst in O_2-saturated 0.1 M KOH at 1600 rpm with a scan rate of 5 mV s^{-1}. c) LSV curves of Co@N-PCF-3 (Co^{2+} molar ratio = 0.5) at different rotation rates, the inset figure is the K–L plots of Co@N-PCF-3 at various voltages. d) Comparative K–L plots of Co@N-PCF-1-5 and Pt/C at −0.4 V.

also superior to that of commercial 20% Pt/C in terms of J_L (4.61 mA cm^{-2}), and $E_{1/2}$ (-169 mV vs Ag/AgCl) except the E_{onset} (−33 mV vs Ag/AgCl) (Figure 4a,b and Table S3, Supporting Information). Interestingly, the ORR electrocatalytic activity of Co@N-PCFs characterized by E_{onset} and $E_{1/2}$ (see Figure S9 in the Supporting Information) first enhanced significantly with the increase of Co content but then decreased slightly, indicating that Co doping can effectively improve the catalytic activity of Co@N-PCFs due to the increased reactive sites. However, the pore volume and specific surface area of Co@N-PCFs decrease with the increase of Co content, which influences the catalytic activity of catalysts. Based on the above factors, Co@N-PCF-3 exhibits the best catalytic activity with a certain amount of Co and mesoporous and a larger specific surface area. Surprisingly, the ORR catalytic activity of Co@N-PCFs in this work acts as one of the most excellent performance compared with previous reports of the best nonprecious metal catalysts derived from ZIF-67 (Table S5, Supporting Information).

For the sake of investigating the ORR mechanism, RDE measurements for all Co@N-PCFs and Pt/C catalysts at various rotation speed from 400 to 1600 rpm were performed and the pertinent kinetic parameters, as well as the electrons transfer number (n)[44] were calculated by the Koutecky–Levich (K–L) equation. As shown in Figure 4c and Figures S10 and S11 (Supporting Information), the J_L of all electrocatalysts improved with the increase of rotation rate due to the decrease of diffusion distance. The linearity and parallelism of K–L plots for all the samples suggest a first-order reaction kinetics and a similar

n value at different potentials (Figure 4d and Figures S10 and S11, Supporting Information). Comparing the slops and intercepts of K–L plots at −0.4 V for all samples (Figure 4d), Co@N-PCF-3 obviously presents the best kinetic activity. The n values of Co@N-PCF-3 (as shown in Table S4, Supporting Information) were calculated to be ≈3.9 range from −0.3 to −0.7 V versus Ag/AgCl, which is higher than those of Co@N-PCF-1 (≈3.28), Co@N-PCF-2 (≈3.80), Co@N-PCF-4 (≈3.90), Co@N-PCF-5 (≈3.85), and Pt/C (≈3.85), indicating that their ORR process mainly involves one-step four-electron transfer pathway ($O_2 + 2H_2O + 4e^- \rightarrow 4OH^-$). Notably, the n values improved with the increase of Co^{2+} molar ratio, signifying that the advisable Co in Co@N-PCFs exhibits an optimum ORR performance.

To gain insights about the catalytic kinetic properties for the prepared electrocatalysts, the Tafel plots were obtained by fitting the Tafel equation from corresponding LSV at 1600 rpm ($\eta = b \log |J_k| + a$, where η is the test potential, $J_k = (J \cdot J_L)/(J - J_L)$, and b is the Tafel slope). It is noteworthy that the Tafel slope for Co@N-PCF-3 (49.45 mV dec^{-1}) is lower than other reference catalysts and 20% Pt/C (80.43 mV dec^{-1}) (Figure S12, Supporting Information) indicating a faster reaction kinetics, which can be further verified by the results of charge transfer resistance obtained by electrochemical impedance spectroscopy (Figure S13, Supporting Information). Impedance diagram demonstrates that Co@N-PCF-3 possesses a smaller semicircle diameter in high-frequency region and a straight line with a larger slope in low-frequency region, indicating a faster electron transfer rate and mass diffusion rate.
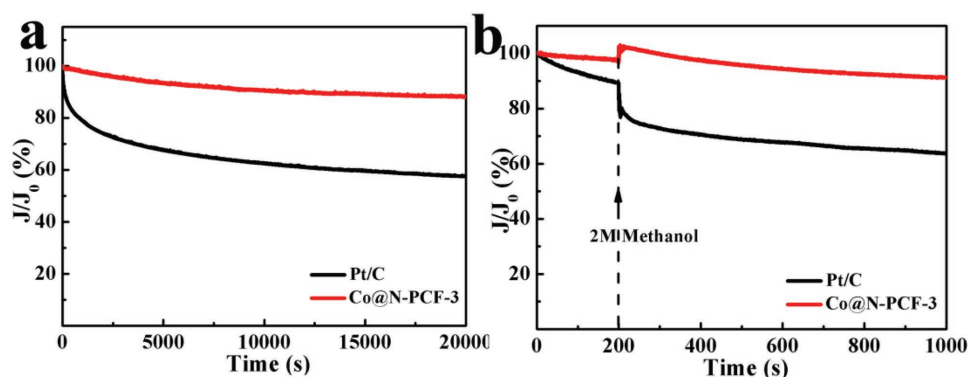
**ADVANCED
SCIENCE NEWS**
www.advancedsciencenews.com

**small
methods**
www.small-methods.com

Figure 5. a) Electrochemical stability and b) methanol tolerance test by current–time (i–t) curves clock reaction for Co@N-PCF-3 and 20% Pt/C at −0.5 V (vs Ag/AgCl) in O_2-saturated 0.1 M KOH electrolyte at 1600 rpm.

Based on the excellent performance of Co@N-PCF-3, the impact of different carbonization temperature (800 °C, 1000 °C) on the ORR electrocatalytic activity of Co@N-PCF-6 and Co@N-PCF-7 was evaluated. Their CVs and LSVs at 1600 rpm were compared in Figure S14 (Supporting Information) and the specific data are listed in Table S3 (Supporting Information). The relatively inferior ORR electrocatalytic activity of Co@N-PCF-6 and Co@N-PCF-7 was observed from the lower E_{onset} (−71, −69 mV) and $E_{1/2}$ (−146, −146 mV), associated with a nethermore J_L (4.33, 4.60 mA cm^{-2}). In addition, their K–L plots and electron transfer number indicated the much poor kinetic activity and the coexistence of the two pathways (multi-step two-electron pathway and one-step four-electron pathway). The catalytic performance of Co@N-PCF-6 inferior to Co@N-PCF-3 maybe due to the lower specific surface area and graphitization extents, which attributed to the fact that partly Zn achieved to volatilize and create the pore texture at 800 °C. Likewise, the ORR catalytic activity of Co@N-PCF-7 is still inferior to Co@N-PCF-3 although the graphitization degree and crystallinity improved with the increase of pyrolysis temperature, which due to the lower BET surface area, less metal active sites (measured by inductively coupled plasma optical emission spectroscopy) and the decreased content of N.[45,46]

On the basis of the above results, Co@N-PCF-3 indicates the most efficient catalytic activity and kinetic activity. However, two other significant parameters (the durability and the methanol tolerance capability) in addition to catalytic activity play a decisive role in the practical application. The electrochemical durability of Co@N-PCF-3 was examined with chronoamperometric (i–t) at −0.5 V (vs Ag/AgCl) in O_2-saturated 0.1 M KOH alkaline electrolyte at 1600 rpm, as well as that of the commercial Pt/C for comparison. As shown in **Figure 5**a, the Co@N-PCF-3 exhibited excellent stability (remains 88.2% of its foremost current density) after 20 000 s of continuous operation, which prevails over that of Pt/C (only 57.5% retention). Moreover, the methanol crossover experiment was also performed by adding 2 M methanol in the same test conditions as the stability test (Figure 5b). A negligible fluctuation in current density for Co@N-PCF-3 was observed in sharp contrast to that of Pt/C, whose ORR current dropped rapidly when methanol was added into alkaline electrolyte, suggesting an outstanding methanol tolerance of Co@N-PCF-3 outperforming the commercial Pt/C.

In order to further verify the advantages of the porous fibers structure for Co@N-PCF-3 from electrospinning, the ORR performance of Co-N-C obtained by direct carbonization of $Zn_{0.5}Co_{0.5}$-ZIF was studied for comparison. The ORR electrocatalytic activity and K–L plots were investigated in Figure S16 (Supporting Information). Co-N-C presented relatively poor electrocatalytic activity and kinetic activity demanding the $E_{1/2}$ of −136 mV, the J_L of 4.6 mA cm^{-2}, and the n values of 3.6, largely due to the collapse of the MOFs skeleton and aggregate in the pyrolysis process (Figure S15b, Supporting Information). The above results fully demonstrated the significance of fibers substrate and high conductivity derived from the 1D continuous fibers linked carbon and Co.

Based on the above ORR performance test results, basic characterization, and previous studies, the outstanding ORR electrochemical, kinetic activity, durability, and methanol tolerance of Co@N-PCF-3 maybe derived from the following important aspects. First, the porous texture and larger specific surface area, derived from the Zn^{2+} of $Zn_{0.5}Co_{0.5}$-ZIF@PAN fiber reduced to Zn by carbonization and evaporated at 900 °C, provide many active sites to contact electrolyte facilitating the ORR. Second, Co-N$_x$ active sites and the types of N species, in which the pyridinic N and the graphitic N play a significant role in improving the E_{onset} and J_L, while the pyrrolic N and the oxidized N have little or no effect on the ORR activity. Third, the graphitic carbon, Co nanoparticles, and 1D fibrous structure, improved the electron and mass conductivity. The synergistic effects of the above contribute to the best ORR performance of Co@N-PCF-3.

3. Conclusion

In summary, 1D Zn_xCo_{1-x}-ZIF@PAN fibers have been successfully prepared by a facile electrospinning method with BMZIFs as precursors to afford uniform Co nanoparticles encapsulated in N-doping mesoporous carbon fibers (Co@N-PCFs) by a subsequent carbonization process. By adjusting the x value in Zn_xCo_{1-x}-ZIFs, the porous texture, the content of Co NPs, and the degree of graphitization of the porous carbon fibers can be well controlled. The most representative Co@N-PCF-3, 1D $Zn_{0.5}Co_{0.5}$-ZIF@PAN fibers carbonization at 900 °C, exhibited the best oxygen reduction electrocatalytic

**ADVANCED
SCIENCE NEWS**
www.advancedsciencenews.com

**small
methods**
www.small-methods.com

activity in the series of catalysts, which even outperforms commercial 20% Pt/C and most of reported catalysts. What is noteworthy is that the Co@N-PCF-3 also exhibits good stability and outstanding methanol crossover effect in 0.1 M KOH electrolyte. The excellent performance of Co@N-PCF-3 is considered to the collaborative role of the mesoporous texture, 1D fibrous structure, larger specific surface area, high graphitization degree, abundant active sites derived from Co-N$_x$ and the higher content of graphitic-N and pyridinic-N and superior electron and mass conductivity. This efficient strategy of electrospinning MOFs based carbon fibers is promising to broaden the research methods for the preparation of efficient electrocatalysts applicated in fuel cells, supercapacitors, and batteries.

Supporting Information

Supporting Information is available from the Wiley Online Library or from the author.

Conflict of Interest

The authors declare no conflict of interest.

[1] J. S. Lee, G. Nam, J. Sun, S. Higashi, H. W. Lee, S. Lee, W. Chen, Y. Cui, J. Cho, *Adv. Energy Mater.* **2016**, *6*, 1601052.

[2] C. Tang, B. Wang, H. F. Wang, Q. Zhang, *Adv. Mater.* **2017**, *29*, 1703185.

[3] C. Van Pham, M. Klingele, B. Britton, K. R. Vuyyuru, T. Unmuessig, S. Holdcroft, A. Fischer, S. Thiele, *Adv. Sustainable Syst.* **2017**, *1*, 1600038.

[4] W. Xiao, J. Zhu, L. Han, S. Liu, J. Wang, Z. Wu, W. Lei, C. Xuan, H. L. Xin, D. Wang, *Nanoscale* **2016**, *8*, 14793.

[5] K. Jiang, P. Wang, S. Guo, X. Zhang, X. Shen, G. Lu, D. Su, X. Huang, *Angew. Chem., Int. Ed.* **2016**, *55*, 9030.

[6] C. Meng, T. Ling, T. Y. Ma, H. Wang, Z. hu, Y. Zhou, J. Mao, X. W. Du, M. Jaroniec, S. Z. Qiao, *Adv. Mater.* **2016**, *29*, 1604607.

[7] K. Iwase, T. Yoshioka, S. Nakanishi, K. Hashimoto, K. Kamiya, *Angew. Chem., Int. Ed.* **2015**, *54*, 11068.

[8] A. Miura, C. Rosero-Navarro, Y. Masubuchi, M. Higuchi, S. Kikkawa, K. Tadanaga, *Angew. Chem., Int. Ed.* **2016**, *55*, 7963.

[9] J. Yang, H. Sun, H. Liang, H. Ji, L. Song, C. Gao, H. Xu, *Adv. Mater.* **2016**, *28*, 4606.

[10] R. Wang, X. Y. Dong, J. Du, J. Y. Zhao, S. Q. Zang, *Adv. Mater.* **2017**, 1703711.

[11] S. M. Unni, J. M. Mora-Hernandez, S. Kurungot, N. Alonso-Vante, *ChemElectroChem* **2015**, *2*, 1339.

[12] S. H. Ahn, X. Yu, A. Manthiram, *Adv. Mater.* **2017**, *29*, 1606534.

[13] F. Hu, H. Yang, C. Wang, Y. Zhang, H. Lu, Q. Wang, *Small* **2017**, *13*, 1602507.

[14] Q. Lai, J. Zhu, Y. Zhao, Y. Liang, J. He, J. Chen, *Small* **2017**, *13*, 1700740.

[15] C. H. Choi, W. S. Choi, O. Kasian, A. K. Mechler, M. T. Sougrati, S. Brüller, K. Strickland, Q. Jia, S. Mukerjee, K. J. J. Mayrhofer, F. Jaouen, *Angew. Chem., Int. Ed.* **2017**, *56*, 8809.

[16] M. Zhang, Q. Dai, H. Zheng, M. Chen, L. Dai, *Adv. Mater.* **2018**, *30*, 1705431.

[17] L. Yang, X. Zeng, W. Wang, D. Cao, *Adv. Funct. Mater.* **2017**, *28*, 1704537.

[18] Z. Li, H. Sun, L. Wei, W. J. Jiang, M. Wu, J. S. Hu, *ACS Appl. Mater. Interfaces* **2017**, *9*, 5272.

[19] M. Wu, K. Wang, M. Yi, Y. Tong, Y. Wang, S. Song, *ACS Catal.* **2017**, *7*, 6082.

[20] T. Zhou, Y. Du, S. Yin, T. Xuezeng, H. Yang, X. Wang, B. Liu, H. Zheng, S. Qiao, R. Xu, *Energy Environ. Sci.* **2016**, *9*, 2563.

[21] W. Xia, C. Qu, Z. Liang, B. Zhao, S. Dai, B. Qiu, Y. Jiao, Q. Zhang, X. Huang, W. Guo, D. Dang, R. Zou, D. Xia, Q. Xu, M. Liu, *Nano Lett.* **2017**, *17*, 2788.

[22] Y. Li, B. Jia, Y. Fan, K. Zhu, G. Li, C. Y. Su, *Adv. Energy Mater.* **2017**, *7*, 1702048.

[23] X. Wang, X. Fan, H. Lin, H. Fu, T. Wang, J. Zheng, X. Li, *RSC Adv.* **2016**, *6*, 37965.

[24] B. You, N. Jiang, M. Sheng, W. S. Drisdell, J. Yano, Y. Sun, *ACS Catal.* **2015**, *5*, 7068.

[25] Z. W. Hu, Z. P. Zhang, Z. L. Li, M. L. Dou, F. Wang, *ACS Appl. Mater. Interfaces* **2017**, *9*, 16109.

[26] B. Bayatsarmadi, Y. Zheng, A. Vasileff, S. Z. Qiao, *Small* **2017**, *13*, 1700191.

[27] L. F. Chen, Y. Lu, L. Yu, X. W. Lou, *Energy Environ. Sci.* **2017**, *10*, 1777.

[28] L. J. Zhang, Z. X. Su, F. L. Jiang, L. L. Yang, J. J. Qian, Y. F. Zhou, W. M. Li, M. C. Hong, *Nanoscale* **2014**, *6*, 6590.

[29] W. Zhang, Z. Y. Wu, H. L. Jiang, S. H. Yu, *J. Am. Chem. Soc.* **2014**, *136*, 14385.

[30] Z. H. Li, M. F. Shao, L. Zhou, Q. H. Yang, C. Zhang, M. Wei, D. G. Evans, X. Duan, *Nano Energy* **2016**, *25*, 100.

[31] Z. H. Li, M. F. Shao, L. Zhou, R. K. Zhang, C. Zhang, M. Wei, D. G. Evans, X. Duan, *Adv. Mater.* **2016**, *28*, 2337.

[32] L. Wang, X. Feng, L. Ren, Q. Piao, J. Zhong, Y. Wang, H. Li, Y. Chen, B. Wang, *J. Am. Chem. Soc.* **2015**, *137*, 4920.

[33] Q. Niu, J. Guo, B. Chen, J. Nie, X. Guo, G. Ma, *Carbon* **2017**, *114*, 250.

[34] M. Q. Zhao, Q. Zhang, J. Q. Huang, F. Wei, *Adv. Funct. Mater.* **2012**, *22*, 675.

[35] W. Zhang, X. Jiang, X. Wang, Y. V. Kaneti, Y. Chen, J. Liu, J. S. Jiang, Y. Yamauchi, M. Hu, *Angew. Chem., Int. Ed.* **2017**, *56*, 8435.

[36] Y. Liu, G. Han, X. Zhang, C. Xing, C. Du, H. Cao, B. Li, *Nano Res.* **2017**, *10*, 3035.

[37] F. C. Shen, Y. Wang, Y. J. Tang, S. L. Li, Y. R. Wang, L. Z. Dong, Y. F. Li, Y. Xu, Y. Q. Lan, *ACS Energy Lett.* **2017**, *2*, 1327.

[38] Y. J. Tang, C. H. Liu, W. Huang, X. L. Wang, L. Z. Dong, S. L. Li, Y. Q. Lan, *ACS Appl. Mater. Interfaces* **2017**, *9*, 16977.

[39] X. Zhou, Y. J. Gao, S. W. Deng, S. Cheng, S. H. Zhang, H. Hu, G. L. Zhuang, X. Zhong, J. G. Wang, *Ind. Eng. Chem. Res.* **2017**, *56*, 11100.

[40] G. T. Fu, Z. M. Cui, Y. F. Chen, Y. T. Li, Y. W. Tang, J. B. Goodenough, *Adv. Energy Mater.* **2017**, *7*, 1601172.

[41] W. H. He, C. H. Jiang, J. B. Wang, L. H. Lu, *Angew. Chem., Int. Ed.* **2014**, *53*, 9503.

[42] R. Li, Z. D. Wei, X. L. Gou, *ACS Catal.* **2015**, *5*, 4133.

[43] G. A. Ferrero, K. Preuss, A. B. Fuertes, M. Sevilla, M. M. Titirici, *J. Mater. Chem. A* **2016**, *4*, 2581.

[44] R. Zhou, Y. Zheng, M. Jaroniec, S. Qiao, *ACS Catal.* **2016**, *6*, 4720.

[45] C. Liu, J. Wang, J. Li, J. Liu, C. Wang, X. Sun, J. Shen, W. Han, L. Wang, *J. Mater. Chem. A* **2017**, *5*, 1211.

[46] L. Shang, H. Yu, X. Huang, T. Bian, R. Shi, Y. Zhao, G. I. N. Waterhouse, L. Z. Wu, C. H. Tung, T. Zhang, *Adv. Mater.* **2016**, *28*, 1668.